Ab initio study of the fracture energy of LiFePO$_4$/FePO$_4$ interfaces

Jongboo Jung [a,b], Maenghyo Cho [a], Min Zhou [a,b],*

[a] WCU Program on Multiscale Mechanical Design, Department of Mechanical and Aerospace of Engineering, Seoul National University, Seoul 151-742, Republic of Korea
[b] George W. Woodruff School of Mechanical Engineering, School of Materials Science and Engineering, Georgia Institute of Technology, Atlanta, GA 30332-0405, USA

HIGHLIGHTS

- Work of separation of (100) and (010) LiFePO$_4$/FePO$_4$ interfaces are quantified.
- Energetically favored modes of separation of the interfaces are identified.
- Relevant surface energies are evaluated.
- Separation along interfaces is more likely than cleavage inside the bulk phases.
- Findings are consistent with experimental observations.

ARTICLE INFO

ABSTRACT

The structure and works of separation of LiFePO$_4$/FePO$_4$ interfaces, interfacial energies, and relevant surface energies are evaluated using *ab initio* calculations based on the density functional theory (DFT). The calculations concern various modes of separation of (100) and (010) interfaces which result in stoichiometric and non-stoichiometric surfaces. Corresponding interfacial fracture toughnesses are calculated based on the works of separation. The analysis reveals the most stable separation configurations and quantifies the cleavage energies. The findings can be used to explain the fracture behavior observed in experiments.

© 2013 Elsevier B.V. All rights reserved.

1. Introduction

Since first introduced in 1997 by Padhi et al. [1], LiFePO$_4$ has been a promising material for lithium ion battery electrodes because of its low cost, high energy density, non-toxicity, abundance in nature, and remarkable thermal stability. Extensive research has been carried out for its practical application in battery systems [1,2]. Despite its advantageous characteristics, drawbacks such as low electric conductivity and capacity fading have hindered its practical usage [3–6]. Various measures such as carbon coating, impurity doping, and particle size reduction have yielded electrochemical performance enhancements [7–10]. One of the main issues which cause degradation of cyclic performance is fracture.

Wang et al. observed cracks in LiFePO$_4$ particles during cycling which lead to poor electric contact and capacity fading [11]. Chen et al. confirmed crack formation in the *bc* planes with aligned dislocations via TEM images [12]. In the work of Habrisch et al., fracture is observed on the surfaces parallel to *bc* planes in chemical delithiation and *bc* and *ac* planes in electrochemical cycling [13]. Ramana et al. observed that dislocations are involved in various interfaces between the two phases along low-index directions which include in *a* and *b* directions in partially delithiated LiFePO$_4$ particles. The topology of the domains depends on the size of samples or how samples are treated [13,14]. These observations showed that cracks are generated along LiFePO$_4$/FePO$_4$ phase boundaries where plastic deformation involving dislocation lines occurs. Indeed, recent studies revealed that no significant capacity fading is observed after cycling in nano-sized particles due to the absence of two-phase coexistence in the particles [15,16]. A continuum analysis based on fracture mechanics predicts the maximum allowable energy release rate and critical particle size for

* Corresponding author. George W. Woodruff School of Mechanical Engineering, Georgia Institute of Technology, Atlanta, GA 30332-0405, USA. Tel.: +1 404 894 3294; fax: +1 404 894 0186.
  E-mail address: min.zhou@gatech.edu (M. Zhou).

which no crack can propagate [17]. The coexistence of the two phases in nanocrystallites is studied analytically using *ab initio* data as input [18].

To design more reliable electrodes, it is necessary to accurately understand how fracture occurs and how the structure of materials affects the fracture behavior of $LiFePO_4/FePO_4$. In the battery system, both crack initiation and subsequent propagation significantly affect performances. Cheng et al. [19] suggested a fracture initiation criterion in Lithium ion battery electrodes by equating the maximum tensile stress to the fracture strength of materials. They proposed that the electrochemical Biot number, which represents the ratio between the charging–discharging current rate and the diffusivity, strongly affects the distribution of stresses in the electrodes. Crack initiation in electrodes may be dominated by the Biot number, the external dynamic condition, and the fracture strength which is an inherent material property. Recently, continuum-level theories have been developed to quantify the coupled chemical and mechanical driving forces for fracture [20,21]. These theories require certain basic material properties such as fracture energy, interfacial energy and surface energy as input. Meanwhile, Density functional theory (DFT) calculations can provide important material property information for determining fracture characteristics from the nature of atomic structures and bonding. Since the mechanical properties of an interface are determined by the chemical bonding at the interface, studies of the structure and properties go hand in hand and DFT can be an important means to quantify the structure and mechanical behavior of materials. DFT analyses have yielded the fracture energies of various interfaces in metals and ceramics and between metals and ceramics [22–30]. The critical data obtained from these calculations can serve as input for higher-scale atomistic (such as molecular dynamics) simulations or continuum analyses. Here, we analyze the structure and energy characteristics of $LiFePO_4/FePO_4$ interfaces for which fracture is an important issue. The analysis focuses on interfaces parallel to the *bc* or *ac* ((100) or (010)) planes where cracks have been and are most likely to be observed. Although plastic deformation through dislocation generation may occur in separation processes, our analysis concerns the attributes of ideal interfaces without plasticity. Such a study provides both important quantification of the work of separation which so far has not been available and understanding of the mechanisms of cleavage failure of the interfaces.

2. Background

2.1. Structures

$LiFePO_4$ and its delithiated structure, $FePO_4$, crystallize in the olivine structure (space group 62, *Pnma*). In this structure, a PO_4 tetrahedron shares an edge and two corners with FeO_6 octahedra which consist of layers in *bc* plane. This construction creates channels along the [010] direction through which Li ions intercalate and diffuse. Fig. 1 illustrates the crystalline structures of $LiFePO_4$ and $FePO_4$. These graphical representations and others to come in this paper are generated using the VESTA visualization software program [31].

Recent experimental observation suggests that $LiFePO_4/FePO_4$ interfaces are the juxtapositions of the two end members ($FePO_4$ and $LiFePO_4$) instead of solid solutions [32]. Although a solid solution might exist under particular conditions, e.g. at, high temperatures [33] or in nano-sized particles [34], our study here focuses on the general case in which the phase boundary consists of two distinct phases on the two sides of (100) and (010) planes.

2.2. Interface properties

The work of separation W_{sep} is a fundamental material property determining the mechanical and thermodynamic properties of an interface. It is defined as the reversible work required to cleave an interface into two pieces of semi-infinite crystals (e.g., A and B) with their respective free surfaces [35], i.e.,

$$W_{sep} = [E_A + E_B - E_{int}]/2S. \tag{1}$$

here, E_{int} is the total energy of the system containing the interface, E_A and E_B are the energies of the A phase and the B phase in their equilibrium states after full separation, respectively. S is the area of the interface. Numerically, the calculation of E_A or E_B can be carried out by replacing the other phase with vacuum in the same supercell as the full interface system. The definition of the properties neglects plastic deformation and diffusion. The work of separation is the dominating factor determining the critical stress for crack propagation in the Griffith equation [36], i.e.,

$$\sigma_F = \left(\frac{W_{sep}E}{\pi c}\right)^{1/2}, \tag{2}$$
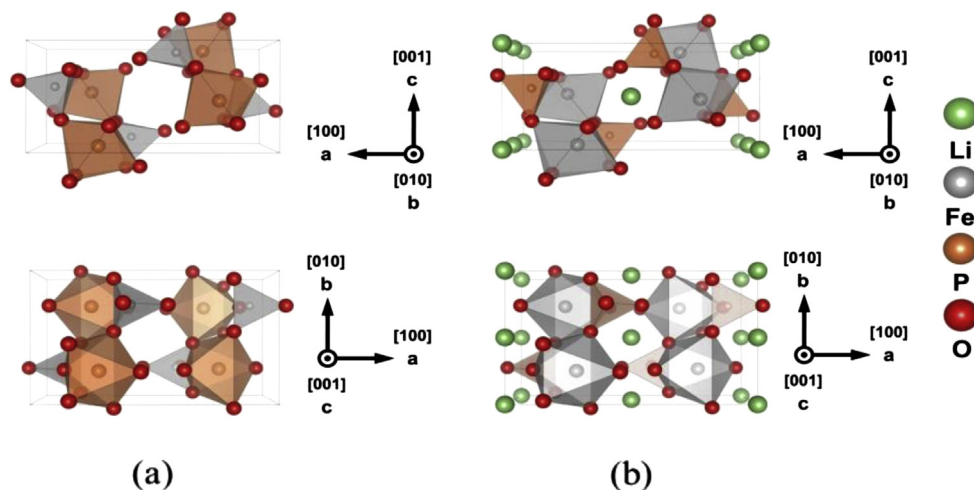
Fig. 1. Crystal structures of (a) $FePO_4$ and (b) $LiFePO_4$. Li atoms are green, Fe atoms are silver, P atoms are brown, and O atoms are red. (For interpretation of the references to color in this figure legend, the reader is referred to the web version of this article.)

where σ_F is the critical stress required to initiate the fracture process, E is the Young's modulus, and c is the crack length. As the most important parameter determining the critical stress, the work of separation is directly linked to fracture dynamics. In crack systems where plastic deformation is involved, the fracture energy can be expressed as the sum of the work of separation and plastic dissipation, i.e., [36,37]

$$\Gamma = W_{\text{sep}} + W_{\text{p}}. \tag{3}$$

Even in situations in which plastic deformation is involved, it is known that W_p is dependent on W_{sep} to a large degree since the work of separation affects the stress level which determines plasticity around crack tips [36,37]. In this regard, the work of separation dominates the fracture behavior at interfaces.

Another fundamental material property is the interfacial energy which is defined as the energy required to form an interface from two bulk phases. It quantifies the stability of the interface relative to the single phases. The generalized form of the interfacial energy is [38]

$$\gamma_{\text{int}} = \left[G_{\text{int}}(T,P) - \sum_i N_i \mu_i(T,P) \right] \Big/ 2S, \tag{4}$$

where G_{int} is the Gibbs free energy of the total interface system, μ_i is the chemical potential per atom of component i, and N_i is the number of the ith component atoms in the system. The summation of $N_i\mu_i$ indicates the sum of the corresponding bulk energies for each phase with the same number of atoms in the interface system.

On the other hand, the surface energy describes the stability of a surface. It is defined as the difference between the free energy of surface atoms and that of atoms in the bulk. The generalized form of surface energy is

$$\sigma_{\text{A(B)}} = \left[G_{\text{SA(B)}}(T,P) - \sum_i N_{\text{A(B)}i} \mu_{\text{A(B)}i} \right] \Big/ 2S, \tag{5}$$

where $G_{\text{SA(B)}}$ is the Gibbs free energy of slab A (B), with the two surfaces fully separated by vacuum in the supercell. In solid-state at $T = 0$ K and $P = 0$, PV and entropy contributions to Gibbs free energy are negligible, so Gibbs free energy reduces to the internal energy E which can be evaluated from first-principles calculations. The work of separation, surface energy and interface energy are related through

$$W_{\text{sep}} = \sigma_{\text{A}} + \sigma_{\text{B}} - \gamma_{\text{int}}. \tag{6}$$

3. Computational method

The first-principle calculations carried out are based on the density functional theory (DFT) and use the Vienna *ab initio* Simulation Package (VASP) [39] with the projector augmented-wave (PAW) [40,41] approach and generalized gradient approximation (GGA) exchange correlation functional of Perdew Wang 1991 [42]. A single plane wave energy cut-off of 520 eV is used for all calculations. The first Brillouin zone is sampled for k-space integration using a Monkhorst–Pack grid and appropriate k-point meshes are used to achieve total energy convergence. All calculations are done with spin polarization due to the antiferromagnetic behavior of FePO$_4$ and LiFePO$_4$ at low temperatures [43]. We adopt the GGA + U approach [44,45], which is proven to correct the energy error of the GGA approach in dealing 3d orbitals [46], with $U = 5.3$ eV and $J = 1$ eV, as used by Wang et al. [47] who showed that the choice of single U and J values for both Fe^{2+} and Fe^{3+} produce convergent surface energy values. The structures are fully

relaxed by calculating the Hellmann–Feynman force until the remaining forces acting on the atoms are smaller than 0.03 eV Å^{-1}.

4. Results

### 4.1. Bulk properties and interface systems

The lattice parameters and internal atomic coordinates are optimized using the conjugate gradient algorithm and are listed in Table 1. The lattice parameters of the relaxed bulk systems are $a = 10.4394$ Å, $b = 6.0524$ Å, and $c = 4.7402$ Å for LiFePO$_4$ and $a = 9.9807$ Å, $b = 5.8941$ Å, $c = 4.8693$ Å for FePO$_4$, in good agreement with experimental data [12,43]. The maximum difference is less than 2.1%. The calculated lattice parameters are slightly higher than the experimental values. This is expected since it is well known that the GGA approach tends to overestimate lattice parameters.

Wang et al. conducted theoretical calculations of the structures and properties of stoichiometric surfaces for both of FePO$_4$ and LiFePO$_4$ [47]. Here, we adopt their surface termination cut for stoichiometric surfaces and choices for the thicknesses of the slabs and atomic relaxation layers which are well proven to reproduce converging energy values. In the interface systems considered, atoms in the interior of each phase are frozen to reproduce bulk behavior whereas atoms in the interface region are relaxed. The interface systems consist of a supercell containing a junction of LiFePO$_4$/FePO$_4$ having an interface parallel to the *bc* or *ac* [(100) or (010)] planes. Periodic boundary conditions are used, so each phase is sandwiched by the other phase and the system has two identical interfaces in the supercell. Due to the lattice mismatch between the two phases, one of the phases is strained to match the other to produce a three-dimensional periodic bulk-like interface system under coherent interface approximation. We consider two types of lattice-strained interface systems with the parameters of either LiFePO$_4$ or FePO$_4$ in this regard. In each case, the lattice of LiFePO$_4$ or FePO$_4$ is stretched/compressed in the *bc* plane or *ac* plane (See Fig. 2). The effect of lattice strain on energy is discussed later in this section. Lattice parameters of the supercells are adopted from optimized bulk lattice parameters of LiFePO$_4$ or FePO$_4$ and kept fixed in all calculations. In the interfaces, the amount of Li intercalated should be considered. The amount of Li at a LiFePO$_4$/FePO$_4$ interface cannot be easily determined because it is affected by many factors, including charging rate and plasticity. Nonetheless, we consider two cases as idealizations. The first case involves Li ions fully filling the interface (full-Li intercalation case), and the second case involves only half the number of Li ions compared to the perfect LiFePO$_4$ at the interface (half-Li intercalation case). In the full-Li intercalation case, to analyze the cleavage of the interface into two surfaces, three possible separations with different lithium segregations at the surfaces created are taken into account by considering the symmetry of Li atoms in the crystalline structure. Referred to as configurations 1, 2, and 3, these cases correspond to lithium ions at the interface adhering to the Li-rich phase (LiFePO$_4$), equally distributed to the two phases, and adhering to the Li-poor phase (FePO$_4$), respectively. All three configurations are illustrated in Figs. 3 and 4. Likewise, two

Table 1
Comparison of calculated bulk lattice parameters with data from experiments.

	a (Å)	b (Å)	c (Å)
LiFePO$_4$	10.4394	6.0524	4.7402
Exp. 1 [43]	10.3375	6.0112	4.6950
Exp. 2 [12]	10.334	6.002	4.695
FePO$_4$	9.9807	5.8941	4.8693
Exp. 1	9.7599	5.7519	4.7560
Exp. 2	9.826	5.794	4.784
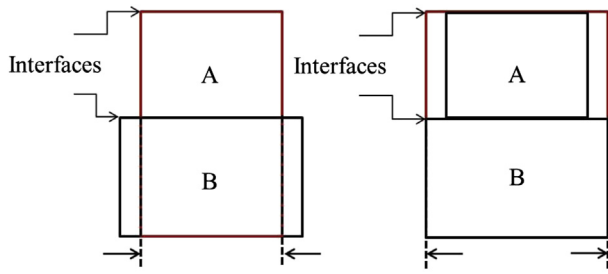
Fig. 2. Model configurations and supercells used. The red boxes illustrate the supercells used in the simulations. One of the phases (LiFePO$_4$ or FePO$_4$) is stretched or expanded to match the other phase's lattice parameters. (For interpretation of the references to color in this figure legend, the reader is referred to the web version of this article.)

configurations corresponding to lithium ions adhering to the Li-rich phase and Li-poor phase are considered in half-Li intercalation case. These configurations are shown in Figs. 5 and 6. For all configurations, the PO$_4$ tetrahedron at the interface is preserved after separation whereas the FeO$_6$ octahedron is not, due to the fact that the breaking of the stronger covalent P–O bond (compared with the Fe–O bond) produces non-stable surfaces [47].

4.2. Surface energy and interfacial energy

For stoichiometric surfaces, $\sum_i N_{A(B)i}\mu_{A(B)i}$ in Equation (5) is the same as the bulk energy of the single phase and it can be simply calculated by evaluating the total energy of a unit cell. In contrast,

the unit cell calculation of bulk energy cannot be used for non-stoichiometric cases due to the lack of periodicity in the structures. Therefore, the surface energy of non-stoichiometric surfaces cannot be obtained easily from *ab initio* calculations of energies and thermodynamic considerations have to be included in the analysis of surface energies of non-stoichiometric systems. However, the range of a surface energy can be established using thermodynamic bounds via the chemical potentials of atoms in the system [38,48–52]. In non-stoichiometric surfaces, the chemical potentials of elements are lower than those of corresponding pure elements in their standalone states. Li is the species causing non-stoichiometry in the systems analyzed here. Therefore, equation (5) reduces to

$$\left.
\begin{aligned}
\sigma_{A(B)} &= \left[G_{SA(B)}(T,P) - \sum_i N_{A(B)i}\mu_{A(B)i} \right]\bigg/ 2S \\
&= \left[E_{slabA(B)} - E_{bulkA(B)} \pm \sum N_{Li}\mu_{Li} \right]\bigg/ 2S,
\end{aligned}
\right\}
\tag{7}$$

where N_{Li} denotes the excess or deficit amount of lithium atoms relative to the stoichiometric bulk structure used to calculate $E_{bulkA(B)}$. The upper bound of μ_{Li} can be set as

$$\mu_{Li} \le \mu_{Li(bulk)}, \tag{8}$$

where $\mu_{Li(bulk)}$ is the elemental bulk chemical potential of lithium. Otherwise, lithium atoms would be precipitated out to their bulk phase on the surfaces. Here, $\mu_{Li(bulk)}$ is taken as the chemical potential of lithium in bcc structure at 0 K ground state. The lower bound can be defined as
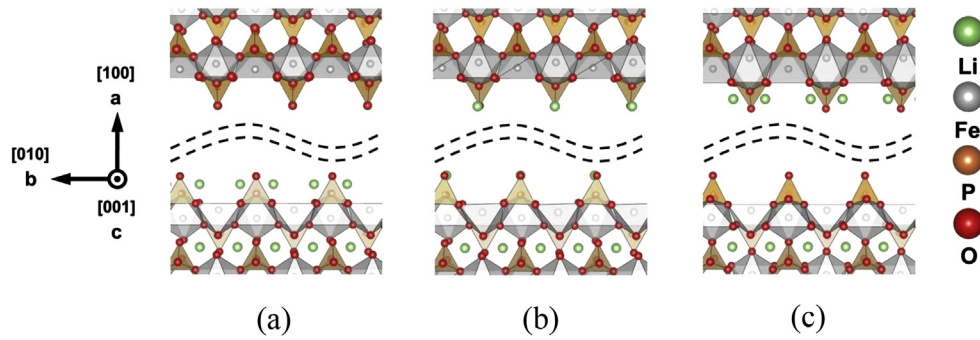
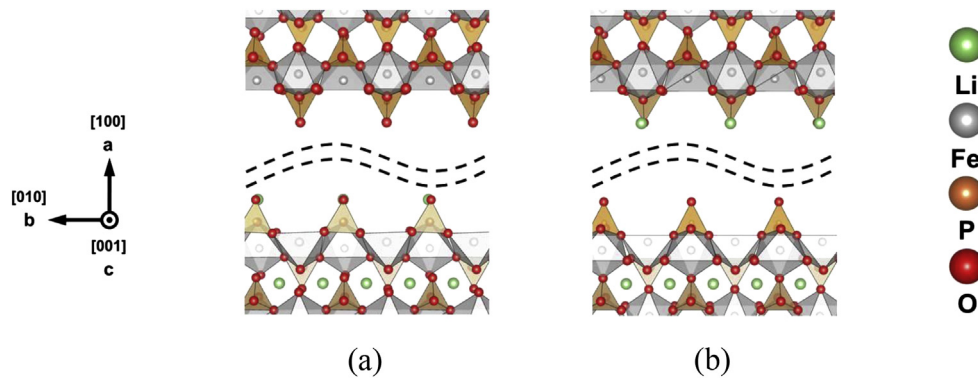**Fig. 3.** Configurations of separated FePO$_4$/LiFePO$_4$ (100) interfaces for full-Li intercalation. The Li-rich phase (LiFePO$_4$) is on lower side and Li-poor phase (FePO$_4$) is on the upper side. Li atoms are green, Fe atoms are silver, P atoms are brown, and O atoms are red. (a) Configuration 1, (b) configuration 2, and (c) configuration 3. (For interpretation of the references to color in this figure legend, the reader is referred to the web version of this article.)
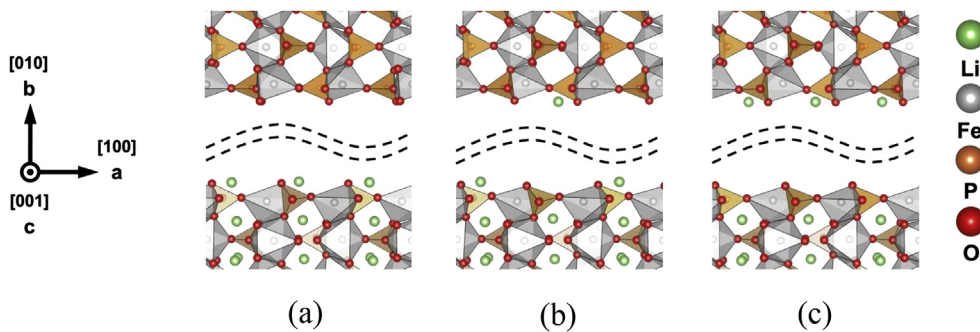
Fig. 4. Configurations of separated FePO$_4$/LiFePO$_4$ (010) interfaces for full-Li intercalation. The Li-rich phase (LiFePO$_4$) is on lower side and Li-poor phase (FePO$_4$) is on the upper side. Li atoms are green, Fe atoms are silver, P atoms are brown, and O atoms are red. (a) Configuration 1, (b) configuration 2, and (c) configuration 3. (For interpretation of the references to color in this figure legend, the reader is referred to the web version of this article.)

Fig. 5. Configurations of separated FePO4/LiFePO4 (100) interfaces for half-Li intercalation. The Li-rich phase (LiFePO4) is on lower side and Li-poor phase (FePO4) is on the upper side. Li atoms are green, Fe atoms are silver, P atoms are brown, and O atoms are red. (a) Configuration 1, and (b) configuration 2. (For interpretation of the references to color in this figure legend, the reader is referred to the web version of this article.)

$$\Delta G + \mu_{\text{Li(bulk)}} \leq \mu_{\text{Li}}, \tag{9}$$

with

$$\Delta G = G_{\text{LiFePO}_4} - G_{\text{FePO}_4} - G_{\text{Li}} \approx E_{\text{LiFePO}_4} - E_{\text{FePO}_4} - E_{\text{Li}}. \tag{10}$$

In the above relations, ΔG is the energy required to form LiFePO$_4$ from crystalline FePO$_4$ and Li per formula unit and G_{LiFePO_4}, G_{FePO_4}, and G_{Li} are the Gibbs free energies per formula unit of LiFePO$_4$, FePO$_4$, and Li which can, respectively, be reduced to E_{LiFePO_4}, E_{FePO_4}, and E_{Li}, the ground state energies evaluated via *ab initio* calculations. The approximation in Equation (10) assumes that the PV and entropy terms in the thermodynamic representation are negligible. In reality, a surface exposed to air can react and produce various compounds according to its environmental conditions, i.e., temperature or partial oxygen pressure. Ong et al. drew phase diagrams based on DFT calculations and characterized them as a function of oxidation conditions [53]. Nevertheless, in this study, we try to

identify a set of bounds for the surface energies through general thermodynamic argument, because accurate DFT calculations for the compounds are quite involved and quantification using phase diagrams is highly dependent on environmental conditions.

The surface energies of (100) and (010) surfaces are listed in Table 2 and plotted as functions of $\Delta\mu_{\text{Li}} = \mu_{\text{Li}} - \mu_{\text{Li(bulk)}}$ in Figs. 7 and 8, respectively. The allowable range of the chemical potential is defined by Equations (8) and (9). For both the (100) and the (010) interfaces, all created surfaces are non-stoichiometric, except for the surface of the Li-poor phase of configuration 1 and the surface of the Li-rich phase of configuration 2. The exact values of the surface energies can only be obtained for stoichiometric surfaces. The surface energies calculated for the stoichiometric surfaces are in good agreement with previously reported values [47]. The averages of the surface energies for Li-poor tend to be lower than those for Li-rich. Here, the calculated surface energies are not sensitive to the applied strain.

The interfacial energy can be calculated in a manner similar to the manner in which the surface energy is calculated above. For half-Li intercalation cases, Equation (4) reduces to

$$\left.\begin{aligned} \gamma_{\text{int}} &= \left[G_{\text{int}}(T,P) - \sum_i N_i \mu_i(T,P) \right] \Big/ 2S \\ &= [E_{\text{int}} - E_{\text{bulkA}} - E_{\text{bulkB}}]/2S, \end{aligned}\right\} \tag{11}$$

where E_{bulkA} and E_{bulkB} are bulk energies of the phases, respectively. The same types of strain as applied in the interfacial structures are applied in the calculations of the bulk energies. In contrast to the half-Li intercalation case, interfacial energies for the full-Li intercalation cases can be expressed as functions of the Li chemical potential because intercalated Li ions produce non-stoichiometric interfaces. This means the interfacial energy lies within the bounds determined by the possible Li chemical potential of the bulk Li-rich phase. Although the chemical potentials of intercalated Li ions are only known by their ranges, the values should be close to the lower limit of Equation (9) due to the fact that intercalated Li ions share analogous atomic bonding states with Li ions in the LiFePO$_4$ crystal. Therefore, it would be reasonable to expect that interfacial energies are closer to the upper bound according to Equation (4). All interfacial energies are listed in Table 3. For full-Li intercalation cases, the ranges of the interfacial energies are listed.

Unlike interfaces consisting of dissimilar compounds, LiFePO$_4$/FePO$_4$ interfaces are comprised of phases sharing analogous structures and chemical bonds. Therefore, the energy difference between the interface and the single bulk phases can be expected to be relatively low. Indeed, for (100) interface, the absolute values of the

Table 2
Surface energies.

Surface	Configuration	Lattice	σ (J m^{-2})	Ref. [47]
Li-rich (100)	1	LiFePO$_4$	1.53 (0.53–2.52)	
		FePO$_4$	1.62 (0.62–2.61)	
	2	LiFePO$_4$	0.64	0.66
		FePO$_4$	0.64	
	3	LiFePO$_4$	1.83 (0.83–2.82)	
		FePO$_4$	1.82 (0.82–2.81)	
Li-rich (010)	1	LiFePO$_4$	1.08 (0.50–1.65)	
		FePO$_4$	1.15 (0.56–1.74)	
	2	LiFePO$_4$	0.63	0.64
		FePO$_4$	0.65	
	3	LiFePO4	1.03 (0.45–1.60)	
		FePO$_4$	1.08 (0.49–1.66)	
Li-poor (100)	1	LiFePO4	1.02	
		FePO$_4$	0.92	0.92
	2	LiFePO$_4$	−0.17 (−1.16 to 0.83)	
		FePO$_4$	−0.26 (−1.25 to 0.74)	
	3	LiFePO$_4$	−0.17 (−2.15 to 1.82)	
		FePO$_4$	−0.19 (−2.17 to 1.80)	
Li-poor (010)	1	LiFePO$_4$	0.36	
		FePO$_4$	0.24	0.24
	2	LiFePO$_4$	−0.09 (−0.66 to 0.49)	
		FePO$_4$	−0.16 (−0.74 to 0.43)	
	3	LiFePO$_4$	−0.48 (−1.63 to 0.67)	
		FePO$_4$	−0.54 (−1.71 to 0.64)	

"Lattice" denotes the lattice parameter for the direction perpendicular to the interface. For non-stoichiometric surfaces, both the average value and the range of the surface energies are given (range is in the parentheses).
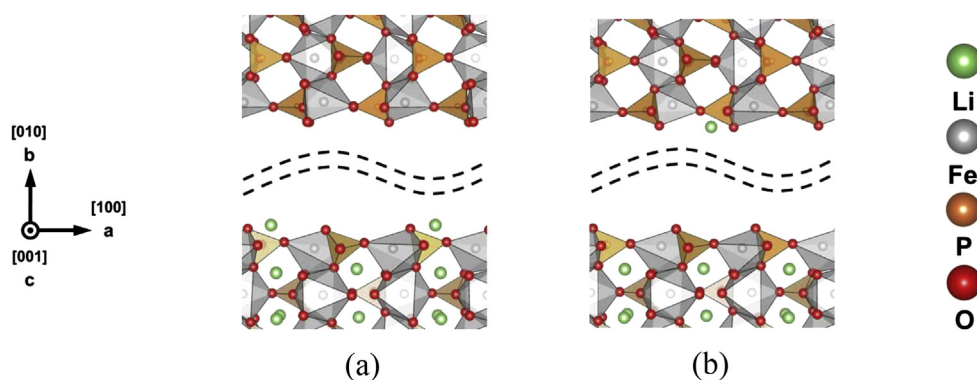
Fig. 6. Configurations of separated FePO4/LiFePO4 (010) interfaces for half-Li intercalation. The Li-rich phase (LiFePO4) is on the lower side and Li-poor phase (FePO4) is on the upper side. Li atoms are green, Fe atoms are silver, P atoms are brown, and O atoms are red. (a) Configuration 1, and (b) configuration 2. (For interpretation of the references to color in this figure legend, the reader is referred to the web version of this article.)
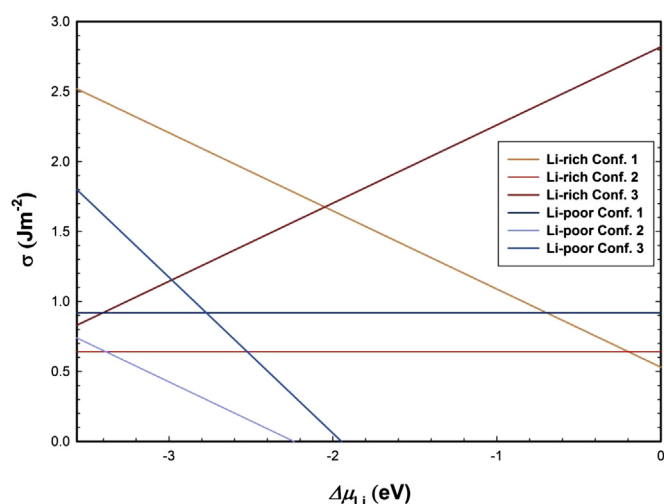
Fig. 7. Surface energies as a function of $\Delta\mu_{Li}$ for the (100) surface.

interfacial energies are generally lower than the surface energies as well as the works of separation, which will be discussed in the next section, confirming that the surface energies have more influence on the fragility of the interfaces considered and the effects of the
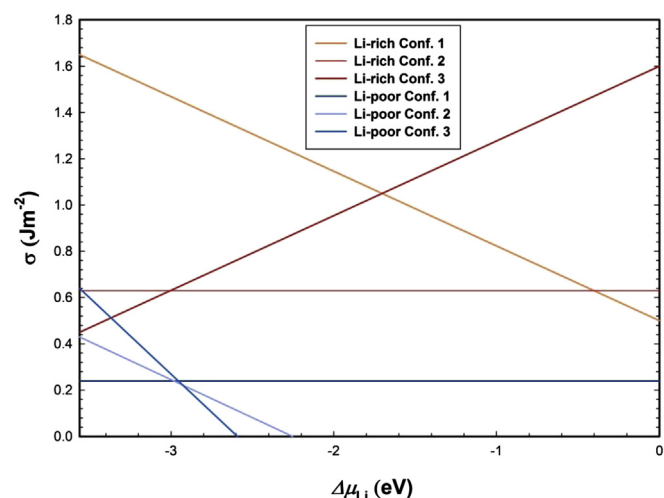
Fig. 8. Surface energies as a function of $\Delta\mu_{Li}$ for the (010) surface.

difference in the nature of the bonding between the phases on fracture are relatively small. However, interfacial energies of the (010) interface are higher than those of the (100) interface and even similar to the works of separation of the interface. One of the causes for this result can be attributed to the higher elastic energy of the (010) interface induced by lattice mismatch. Indeed, the elastic energy increment during stretch perpendicular to the (010) plane is higher than that for stretch perpendicular to the (100) plane in both LiFePO4 and FePO4. In particular, the total energy increase is 1.4% for straining perpendicular to the (010) plane whereas and is negligible for straining perpendicular to the (100) plane.

4.3. Work of separation

The works of separation for each of the three possible configurations and both types of lattice straining are listed in Table 4. For the (100) interface, configuration 2, which has Li equally split between the two sides, possesses the lowest work of separation of 1.18 (1.14) J m^{-2} among the three configurations. The number in parentheses denotes the value evaluated using the lattice parameters of FePO4 whereas that not in parentheses is evaluated using the lattice parameters of LiFePO4. This result suggests that this configuration is the most likely fracture mode under idealized circumstances. The cleavage energy, W_{cleave}, for a single phase is defined similarly as work of separation. It can be expressed as twice the surface energy, i.e., $W_{cleave} = 2\sigma$ with σ being the surface energy of a cleaved plane. From the stoichiometric surface energies of the (100) planes of FePO4 and LiFePO4, it can be deduced that

$$W_{cleave(FePO_4)} > W_{cleave(LiFePO_4)} > W_{sep}.$$

The separation between FePO4 and LiFePO4 requires a lower amount of energy compared with the separation of each of the two pure phases.

Configurations 2 and 3 for the (010) interface have similar works of separation: 0.72 (0.59) J m^{-2} for configuration 2 and 0.71 (0.63) J m^{-2} for configuration 3. Therefore, both separations are

Table 3
Interfacial energies.

	Lattice	Full-Li bc (100) plane	Full-Li ac (010) plane	Half-Li bc (100) plane	Half-Li bc (100) plane
γ (J m^{-2})	LiFePO4	−1.69 to 0.30	−0.70 to 0.45	0.12	0.53
	FePO4	−1.75 to 0.24	−0.68 to 0.49	0.16	0.49

"Lattice" denotes the lattice parameter for the direction perpendicular to the interface.

Table 4
Works of separation for full-Li intercalation.

Interface	Configuration	Lattice	W_{sep} (J m^{-2})
LiFePO$_4$/FePO$_4$-*bc* (100) plane	1	LiFePO$_4$	3.23
		FePO$_4$	3.29
	2	LiFePO$_4$	1.18
		FePO$_4$	1.14
	3	LiFePO$_4$	2.36
		FePO$_4$	2.39
LiFePO$_4$ single phase		LiFePO$_4$	1.28
FePO$_4$ single phase		FePO$_4$	1.84
LiFePO$_4$/FePO$_4$-*ac* (010) plane	1	LiFePO$_4$	1.60
		FePO$_4$	1.49
	2	LiFePO$_4$	0.72
		FePO$_4$	0.59
	3	LiFePO$_4$	0.71
		FePO$_4$	0.63
LiFePO$_4$ single phase		LiFePO$_4$	1.26
FePO$_4$ single phase		FePO$_4$	0.48

"Lattice" denotes the lattice parameter for the direction perpendicular to the interface. The cleavage energies for the single phases are also listed.

more likely than the separation represented by configuration 1. The work of separation of this interface and the cleavage energies of the corresponding planes in the pure phases follow this order of magnitude:

$$W_{cleave(LiFePO_4)} > W_{sep(conf.2)} > W_{sep(conf.3)} > W_{cleave(FePO_4)}.$$

The cleavage energy for the LiFePO$_4$ phase is the highest, followed by the work of separation (configurations 2 and 3), with the cleavage energy for FePO$_4$ being the lowest. So, for the (010) orientation, cleavage in the FePO$_4$ phase is the most likely to occur, followed by the interfacial separation, with the cleavage in the LiFePO$_4$ phase the least likely to occur. It is important to point out that these results are for idealized conditions and do not account for the effect of plasticity (dislocation generation or twining) at the phase boundary or in the phases.

For the half-Li intercalation, works of separation for all configurations are listed in Table 5. Unlike the case of full-Li intercalation, the energies calculated for all configurations have similar values for both (100) and (010) interfaces. The work of separation of the (100) interface has the same value of 1.54 (1.39) J m^{-2} for each configuration which is higher than the work of separation in the full-Li intercalation case and also higher than the cleavage energy of LiFePO$_4$. Obviously,

$$W_{cleave(FePO_4)} > W_{sep} > W_{cleave(LiFePO_4)}.$$

The works of separation of the (010) interfaces are in the range of 0.41–0.50 J m^{-2}. These are much lower than the cleavage energy of LiFePO$_4$ and even lower than the energy required to cleave the (010) interface with full-Li intercalation. Except the value of configuration 1 calculated with the LiFePO$_4$ lattice parameters, all

Table 5
Works of separation for half-Li intercalation.

Interface	Configuration	Lattice	W_{sep} (J m^{-2})
LiFePO$_4$/FePO$_4$-*bc* (100) plane	1	LiFePO$_4$	1.54
		FePO$_4$	1.39
	2	LiFePO$_4$	1.54
		FePO$_4$	1.39
LiFePO$_4$/FePO$_4$-*ac* (010) plane	1	LiFePO$_4$	0.50
		FePO$_4$	0.41
	2	LiFePO4	0.45
		FePO$_4$	0.43

the works of separation of this interface are slightly lower than the cleavage energy of FePO$_4$.

The work of separation of the (100) interface with full-Li intercalation shows the least dependence on the lattice parameters of the supercell used. In other cases, the energies obtained using the lattice parameters of LiFePO$_4$ tend to be higher. The strain energy generated by the stretch or compression is found to be insignificant compared with the total energies. Specifically, the elastic contribution to the total energy of a single phase is less than 0.3%. However, the strain contribution induced by the lattice mismatch causes the calculated works of separation under different lattice parameters to deviate from each other up to 18%.

Based on Pauling's third rule [54], Gabrisch et al. proposed that separating (100) planes requires higher driving forces than separating (010) planes since corner-sharing bonds between PO$_4$ tetrahedra and FeO$_6$ octahedra in (100) planes have a higher bond strength than the edge-sharing bonds between FeO$_6$ octahedra in (010) planes [13]. This is validated by our result, in which the works of separation for (100) interfaces are higher than those for (010) interfaces.

Fracture toughness is an inherent material property which determines a material's resistance to fracture. Based on the Griffith theory, the elastic driving force for fracture on an equilibrium crack, Γ, can be expressed as

$$\Gamma = \frac{(1-\nu)K_I^2}{2G},$$ (12)

where K_I is the stress intensity factor under mode I loading, ν is Poisson's ratio, and G is shear modulus. For the opening of an interface, the driving force is equal to the difference between the sum of the surface energies of the resulting surfaces ($\sigma_A + \sigma_B$) and the interfacial energy (γ_{int}). This quantity is equal to the work of separation, W_{sep}, according to Equation (6). Therefore, the interfacial fracture toughness, K_g, which is the critical mode I stress intensity factor, is related to the work of separation as

$$K_g = \sqrt{\frac{2GW_{sep}}{(1-\nu)}}.$$ (13)

Although the shear strengths and Poisson's ratios of LiFePO$_4$ and FePO$_4$, differ, their values do not vary significantly from each other [55]. Therefore, the work of separation is the dominant factor determining the interfacial fracture toughness of LiFePO$_4$/FePO$_4$ interfaces. The calculated fracture toughness values for the most stable configuration of each interfaces are listed in Table 6. As seen from the discussion on the work of separation, fracture resistance is lower for the (010) interfaces.

In experiments, fracture surfaces are observed along either (100) or (010) planes where the two phases are adjoined with structures of dislocations [11–14]. In our analysis, the energies required to cleave the (100) interface in the full-Li intercalation case and the (010) interface in the half-Li intercalation case are lower than the single-phase cleavage energies of FePO$_4$ and LiFePO$_4$ even without plasticity effects. The results obtained here can be refined

Table 6
Interfacial Fracture toughness.

	Lattice	Full-Li *bc* (100) plane	Full-Li *ac* (010) plane	Half-Li *bc* (100) plane	Half-Li *ac* (010) plane
K_g (MPa m$^{1/2}$)	LiFePO$_4$	0.40	0.31	0.46	0.25
	FePO$_4$	0.39	0.28	0.43	0.23

"Lattice" denotes the lattice parameter for the direction perpendicular to the interface.

in the future by taking into account plasticity which is beyond the scope of the present study. Corrections should be made if the formation of the interface involves structural modifications such as surface reconstruction, change of lattice type or straining due to incompatible lattice parameters and elastic moduli. The structure of interfaces with lattice mismatches depends on the interplay between interface bonding and lattice straining which often results in the formation of misfit dislocations. Because of the lattice mismatches between $LiFePO_4$ and $FePO_4$, the effect of the misfit strains must be estimated for more accurate results. According to Schnitker et al., the error in energy due to the coherent interface approximation without considering misfit dislocations can be up to the order of tens of percent [56]. The inclusion of misfit dislocations in the supercell in *ab initio* calculation is currently unfeasible because extremely expensive computations are required. One of the approaches in this regard uses the Peierls–Nabarro model [57,58] which is a continuum model commonly used with *ab initio* input. In previous studies using this method, considerably lower energies are obtained with the inclusion of elastic and chemical contributions of misfit energy [27,30,59]. In this regard, it can be expected that lower works of separation of $LiFePO_4/FePO_4$ interfaces may result if misfit dislocations are considered.

5. Conclusion

Energies relevant to the separation of (100) and (010) $LiFePO_4/FePO_4$ interfaces including the ideal work of separation, surface energy, and interfacial energy are quantified using *ab initio* calculations based on the density functional theory (DFT).

Three possible configurations of separation at the interfaces for full-Li intercalation and half-Li intercalation are considered and compared, leading to the identification of the amount of energy required to cleave the interfaces and the energetically-favored surface configurations resulting from separation along these interfaces.

The surface energies for all types of surfaces created from separation of the (100) and (010) planes are calculated. Possible ranges of surface energies for non-stoichiometric surfaces are expressed via allowable chemical potential of Li in the structures.

Interfaces with full-Li intercalation are first considered in our analysis of the work of separation. For the (100) interface, the work of separation is lowest when Li ions are equally split between the two sides and is lower than the corresponding cleavage energies of the single phases. For the (010) interface, configurations 2 and 3 have similar works of separation that are lower than that of configuration 1. The cleavage energy for the single phase of $FePO_4$ is lower than this work of separation between the two phases. Interfaces with half-Li intercalation behave somewhat differently from interfaces with full-Li intercalation. For the (100) interface, the work of separation is higher than that with the full-Li intercalation and the cleavage energy of the $LiFePO_4$ single phase. For the (010) interface, the work of separation is similar to the cleavage energy of the $FePO_4$ single phase. The works of separation for all the interfacial separation configurations considered in do not exceed 3.5 J m^{-1} [2], and the energies corresponding to the most stable configuration for each interfaces are in the range of 0.41–1.18 J m^{-1} [2]. Ideal fracture toughnesses also are measured using the works of separation.

Interfacial energies for (100) and (010) interfaces of both types of half-Li and full-Li intercalations are calculated and it is shown that the interfacial energies for (100) interfaces tend to be lower than those of (010) interfaces. A comparison of the surface energies and interfacial energies reveals that the surface energies have dominant contributions to the works of separation for (100) interfaces whereas the interfacial energies also play important roles in determining the work of separation of (010) interfaces.

The study has also shown that separation at interfaces is more likely to occur than cleavage inside the phases along the same crystalline planes, consistent with experimental observations. The quantification given here can provide useful input to studies of fracture, interfaces, and surfaces in $LiFePO_4/FePO_4$ at higher scales.

References

[1] A. Padhi, K. Nanjundaswamy, J.B. Goodenough, Journal of the Electrochemical Society 144 (1997) 1188.
[2] O. Haas, A. Deb, E. Cairns, A. Wokaun, Journal of the Electrochemical Society 152 (2005) A191.
[3] A.S. Andersson, B. Kalska, L. Häggström, J.O. Thomas, Solid State Ionics 130 (2000) 41.
[4] A. Andersson, J. Thomas, Journal of Power Sources 97 (2001) 498.
[5] F. Croce, A. D'Epifanio, J. Hassoun, A. Deptula, T. Olczac, B. Scrosati, Electrochemical and Solid-State Letters 5 (2002).
[6] P. Prosini, M. Carewska, S. Scaccia, P. Wisniewski, S. Passerini, M. Pasquali, Journal of the Electrochemical Society 149 (2002) A886.
[7] N. Ravet, J. Goodenough, S. Besner, M. Simoneau, P. Hovington, M. Armand (1999) 1999.
[8] S. Shi, L. Liu, C. Ouyang, D. Wang, Z. Wang, L. Chen, X. Huang, Physical Review B 68 (2003) 195108.
[9] D. Wang, H. Li, S. Shi, X. Huang, L. Chen, Electrochimica Acta 50 (2005) 2955.
[10] K.F. Hsu, S.Y. Tsay, B.J. Hwang, Journal of Materials Chemistry 14 (2004) 2690.
[11] D. Wang, X. Wu, Z. Wang, L. Chen, Journal of Power Sources 140 (2005) 125.
[12] G. Chen, X. Song, T.J. Richardson, Electrochemical and Solid-State Letters 9 (2006) A295.
[13] H. Gabrisch, J. Wilcox, M.M. Doeff, Electrochemical and Solid-State Letters 11 (2008) A25.
[14] C.V. Ramana, A. Mauger, F. Gendron, C.M. Julien, K. Zaghib, Journal of Power Sources 187 (2009) 555.
[15] C. Delacourt, P. Poizot, S. Levasseur, C. Masquelier, Electrochemical and Solid-State Letters 9 (2006) A352.
[16] P. Gibot, M. Casas-Cabanas, L. Laffont, S. Levasseur, P. Carlach, S. Hamelet, J.M. Tarascon, C. Masquelier, Nature Materials 7 (2008) 741.
[17] K. Zhao, M. Pharr, J.J. Vlassak, Z. Suo, Journal of Applied Physics 108 (2010) 073517.
[18] M. Wagemaker, F.M. Mulder, A. Van der Ven, Advanced Materials 21 (2009) 2703.
[19] Y.-T. Cheng, M.W. Verbrugge, Journal of the Electrochemical Society 157 (2010) A508.
[20] Y. Gao, M. Cho, M. Zhou, Journal of Mechanical Science and Technology 27 (2013) 1505.
[21] Y. Gao, M. Zhou, Journal of Power Sources 230 (2013) 176.
[22] D. Siegel, L. Hector, J. Adams, Physical Review B 67 (2003).
[23] J. Hoekstra, M. Kohyama, Physical Review B 57 (1998) 2334.
[24] I. Batirev, A. Alavi, M. Finnis, T. Deutsch, Physical Review Letters 82 (1999) 1510.
[25] W. Zhang, J. Smith, A. Evans, Acta Materialia 50 (2002) 3803.
[26] W. Zhang, J. Smith, X.G. Wang, A. Evans, Physical Review B 67 (2003) 245414.
[27] N.I. Medvedeva, Y.N. Gornostyrev, O.Y. Kontsevoi, A.J. Freeman, Acta Materialia 52 (2004) 675.
[28] S. Johansson, M. Christensen, G. Wahnström, Physical Review Letters 95 (2005).
[29] W. Liu, J.C. Li, W.T. Zheng, Q. Jiang, Physical Review B 73 (2006).
[30] D. Fors, G. Wahnström, Physical Review B 82 (2010).
[31] G. Henkelman, B.P. Uberuaga, H. Jónsson, Journal of Chemical Physics 113 (2000) 9901.
[32] L. Laffont, C. Delacourt, P. Gibot, M.Y. Wu, P. Kooyman, C. Masquelier, J.M. Tarascon, Chemistry of Materials 18 (2006) 5520.
[33] C. Delacourt, J. Rodríguez-Carvajal, B. Schmitt, J.M. Tarascon, C. Masquelier, Solid State Sciences 7 (2005) 1506.
[34] N. Meethong, H.Y.S. Huang, W.C. Carter, Y.M. Chiang, Electrochemical and Solid-State Letters 10 (2007) A134.
[35] O. Andersen, M. Methfessel, Acta Metallurgica et Materialia 40 (1992) S1.
[36] J.E. Raynolds, J.R. Smith, G.L. Zhao, D.J. Srolovitz, Physical Review B 53 (1996) 13883.
[37] J.R. Rice, Proceedings of the First International Conference on Fracture, Sendai 1 (1966) 309.
[38] I.G. Batyrev, A. Alavi, M.W. Finnis, Physical Review B 62 (2000) 4698.
[39] G. Kresse, J. Furthmüller, Physical Review B 54 (1996) 11169.
[40] G. Kresse, D. Joubert, Physical Review B 59 (1999) 1758.
[41] P.E. Blöchl, Physical Review B 50 (1994) 17953.

[42] J.P. Perdew, J. Chevary, S. Vosko, K.A. Jackson, M.R. Pederson, D. Singh, C. Fiolhais, Physical Review B 46 (1992) 6671.
[43] G. Rousse, J. Rodriguez-Carvajal, S. Patoux, C. Masquelier, Chemistry of Materials 15 (2003) 4082.
[44] V.I. Anisimov, J. Zaanen, O.K. Andersen, Physical Review B 44 (1991) 943.
[45] V.I. Anisimov, F. Aryasetiawan, A. Lichtenstein, Journal of Physics: Condensed Matter 9 (1997) 767.
[46] L. Wang, T. Maxisch, G. Ceder, Physical Review B 73 (2006).
[47] L. Wang, F. Zhou, Y. Meng, G. Ceder, Physical Review B 76 (2007).
[48] S. Zhang, J.E. Northrup, Physical Review Letters 67 (1991) 2339.
[49] K. Johnston, M.R. Castell, A.T. Paxton, M.W. Finnis, Physical Review B 70 (2004) 085415.

[50] K. Rapcewicz, B. Chen, B. Yakobson, J. Bernholc, Physical Review B 57 (1998) 7281.
[51] I. Batyrev, A. Alavi, M.W. Finnis, Faraday Discussions 114 (1999) 33.
[52] Y. Mo, S.P. Ong, G. Ceder, Physical Review B 84 (2011) 205446.
[53] S. Ping Ong, L. Wang, B. Kang, G. Ceder, Chemistry of Materials 20 (2008) 1798.
[54] L. Pauling, Journal of the American Chemical Society 51 (1929) 1010.
[55] T. Maxisch, G. Ceder, Physical Review B 73 (2006).
[56] J. Schnitker, D.J. Srolovitz, Modelling and Simulation in Materials Science and Engineering 6 (1998) 153.
[57] R. Peierls, Proceedings of the Physical Society 52 (1940) 34.
[58] F. Nabarro, Proceedings of the Physical Society 59 (1947) 256.
[59] Y. Yao, T. Wang, C. Wang, Physical Review B 59 (1999) 8232.